

# Spin-Polarized Photocatalytic CO<sub>2</sub> Reduction of Mn-Doped Perovskite Nanoplates

Cheng-Chieh Lin, Ting-Ran Liu, Sin-Rong Lin, Karunakara Moorthy Boopathi, Chun-Hao Chiang, Wen-Yen Tzeng, Wan-Hsiu Chang Chien, Hua-Shu Hsu, Chih-Wei Luo, Hui-Ying Tsai, Hsin-An Chen, Pai-Chia Kuo, Jessie Shiue, Jau-Wern Chiou, Way-Faung Pong, Chia-Chun Chen,\* and Chun-Wei Chen\*



Cite This: *J. Am. Chem. Soc.* 2022, 144, 15718–15726



Read Online

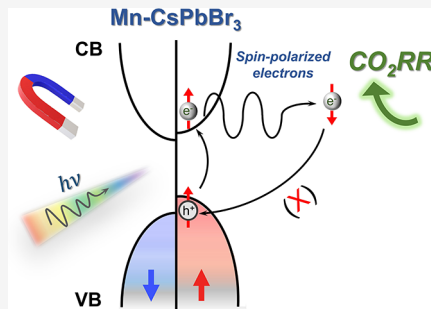
ACCESS |

Metrics & More

Article Recommendations

Supporting Information

**ABSTRACT:** “Spin” has been recently reported as an important degree of electronic freedom to improve the performance of electrocatalysts and photocatalysts. This work demonstrates the manipulations of spin-polarized electrons in CsPbBr<sub>3</sub> halide perovskite nanoplates (NPLs) to boost the photocatalytic CO<sub>2</sub> reduction reaction (CO<sub>2</sub>RR) efficiencies by doping manganese cations (Mn<sup>2+</sup>) and applying an external magnetic field. Mn-doped CsPbBr<sub>3</sub> (Mn-CsPbBr<sub>3</sub>) NPLs exhibit an outstanding photocatalytic CO<sub>2</sub>RR compared to pristine CsPbBr<sub>3</sub> NPLs due to creating spin-polarized electrons after Mn doping. Notably, the photocatalytic CO<sub>2</sub>RR of Mn-CsPbBr<sub>3</sub> NPLs is significantly enhanced by applying an external magnetic field. Mn-CsPbBr<sub>3</sub> NPLs exhibit 5.7 times improved performance of photocatalytic CO<sub>2</sub>RR under a magnetic field of 300 mT with a permanent magnet compared to pristine CsPbBr<sub>3</sub> NPLs. The corresponding mechanism is systematically investigated by magnetic circular dichroism spectroscopy, ultrafast transient absorption spectroscopy, and density functional theory simulation. The origin of enhanced photocatalytic CO<sub>2</sub>RR efficiencies of Mn-CsPbBr<sub>3</sub> NPLs is due to the increased number of spin-polarized photoexcited carriers by synergistic doping of the magnetic elements and applying a magnetic field, resulting in prolonged carrier lifetime and suppressed charge recombination. Our result shows that manipulating spin-polarized electrons in photocatalytic semiconductors provides an effective strategy to boost photocatalytic CO<sub>2</sub>RR efficiencies.



## INTRODUCTION

Artificial photosynthesis using solar-driven CO<sub>2</sub> reduction to value-added fuels and chemicals has attracted great attention recently because it provides a promising strategy for simultaneously tackling two important environmental issues of global warming and renewable energy.<sup>1–4</sup> However, because photocatalytic CO<sub>2</sub> reduction processes involve sluggish multielectron reaction kinetics, until now, the solar-driven CO<sub>2</sub> reduction conversion efficiency is still far from the satisfactory requirement for practical applications.<sup>5,6</sup> Typically, the conversion efficiency of photocatalytic CO<sub>2</sub> reduction is governed by several determining factors such as light-harvesting, CO<sub>2</sub> adsorption, charge separation and transport of photogenerated carriers, and redox reaction.<sup>7,8</sup> Extensive research has been devoted to pursuing efficient photocatalysts for CO<sub>2</sub> reduction by optimizing these key factors among materials.<sup>6,7,9</sup> Halide perovskite semiconductors are an emerging class of solution-processable optoelectronic materials for high-performance solar cells and also for light-emitting diodes (LEDs) because they exhibit superior physical properties such as high optical absorption coefficients, low-cost fabrications, tunable band gaps, long diffusion lengths, and long carrier lifetime.<sup>10–14</sup> Due to its excellent intrinsic

optoelectronic properties, halide perovskites have also recently demonstrated their great potential in photocatalyst applications of solar-driven CO<sub>2</sub> reduction or hydrogen evolution.<sup>15–21</sup> Many efforts have been made to enhance the photocatalytic CO<sub>2</sub> reduction efficiencies and stabilities of halide perovskites.<sup>22–24</sup> For example, it has been known that an effective strategy to enhance the photocatalytic CO<sub>2</sub> reduction efficiency is to construct heterojunctions of halide perovskites with other nanoscale materials to promote charge separation and suppress charge recombination.<sup>18,23,25,26</sup> The creation of built-in electric fields at heterojunctions may significantly enhance the photoinduced carrier separation efficiencies and their corresponding photocatalytic CO<sub>2</sub> reduction performance.<sup>23,25,26</sup>

Received: June 9, 2022

Published: August 17, 2022



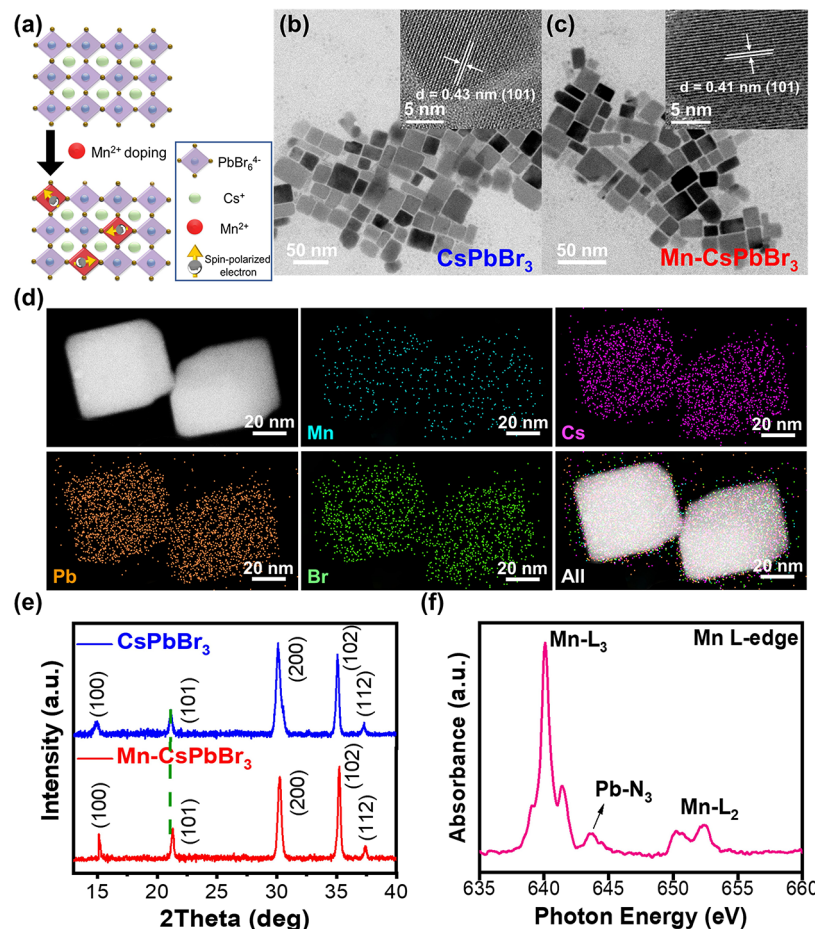


**Figure 1.** Morphology and structural characterization of CsPbBr<sub>3</sub> and Mn-CsPbBr<sub>3</sub> NPLs. (a) Schematic illustration of the formation of the electron spin polarization by doping magnetic Mn<sup>2+</sup> ions in 3D all-inorganic perovskite CsPbBr<sub>3</sub>. The TEM images of (b) CsPbBr<sub>3</sub> and (c) Mn-CsPbBr<sub>3</sub> NPLs. The insets are the HR-TEM images of CsPbBr<sub>3</sub> and Mn-CsPbBr<sub>3</sub> NPLs. (d) The HAADF-STEM and EDS element mapping (Mn, Cs, Pb, and Br) images of Mn-CsPbBr<sub>3</sub> NPLs. (e) The PXRD spectroscopy of CsPbBr<sub>3</sub> (blue) and Mn-CsPbBr<sub>3</sub> NPLs (red). (f) The Mn L<sub>3,2</sub>-edge XANES spectroscopy of Mn-CsPbBr<sub>3</sub> NPLs.

“Spin”, which is the intrinsic characteristic property of electrons, has been recently reported as another important degree of electronic freedom to improve the performance of electrocatalysts and photocatalysts.<sup>4,27–31</sup> Spin selection has been described as a possible way to promote electrocatalytic oxygen evolution reaction (OER), which involves the process of forming triplet-state O<sub>2</sub> from singlet-state species (OH<sup>−</sup> or H<sub>2</sub>O).<sup>32–34</sup> Accordingly, the spin polarization of the active catalyst surface may favor the parallel spin alignment of oxygen atoms during the reaction.<sup>27,33</sup> Inspired by the success of enhanced OER electrocatalytic activity by spin regulation, the manipulation of spin-polarized electrons is also an effective strategy to enhance the photocatalytic activities of materials.<sup>35–37</sup> Because photocatalysis usually requires a rapid charge transfer and a prolonged lifetime of intermediate species for redox reactions, the spin polarizations of photoexcited electrons may play a positive role in the enhanced charge separation and suppression of charge recombination.<sup>35,36</sup> For example, improved hydrogen evolution reaction (HER) and nitrogen reduction reaction (NRR) photocatalytic activities for metal oxides of TiO<sub>2</sub> and BaTiO<sub>3</sub> have been demonstrated recently.<sup>35,37</sup> The generation of spin-polarized electrons by controlling the concentrations of metal or oxygen vacancies in these metal oxides may significantly enhance their photocatalytic activities.<sup>30,35–37</sup> However, although creating vacan-

cies is an effective way to enhance spin-polarized electrons, the formation of traps and defects within the materials may simultaneously hinder the carrier diffusion and transport.<sup>38</sup> By contrast, doping magnetic elements into semiconductors could be another effective strategy to manipulate spin-polarized electrons in photocatalysis without largely sacrificing the crystallinity of the materials.<sup>39–41</sup> Spin coupling of magnetic elements with semiconductors was shown to successfully modify their electronic, optical, and magnetic properties with the aim for spintronic applications.<sup>42–44</sup>

In this work, we demonstrate that the photocatalytic CO<sub>2</sub> reduction conversion efficiencies can be significantly enhanced by manipulating the spin-polarized electrons of halide perovskite CsPbBr<sub>3</sub> nanoplates (NPLs). By doping with the magnetic element Mn, the photocatalytic CO<sub>2</sub> reduction efficiency of Mn-doped CsPbBr<sub>3</sub> (Mn-CsPbBr<sub>3</sub>) NPLs can be significantly enhanced due to the increased spin polarization of photogenerated carriers and suppression of the charge recombination. Notably, the photocatalytic CO<sub>2</sub> reduction efficiencies of Mn-CsPbBr<sub>3</sub> NPLs can be further enhanced by applying an external magnetic field based on a permanent magnet. The Mn-CsPbBr<sub>3</sub> NPLs exhibit a 3.4 and 5.7 times improved performance of the photocatalytic CO<sub>2</sub> reduction reaction (CO<sub>2</sub>RR) under a magnetic field of 100 and 300 mT, respectively, with a permanent magnet compared to the

pristine  $\text{CsPbBr}_3$  NPLs. The origin of the enhanced photocatalytic  $\text{CO}_2$  reduction efficiencies of Mn-CsPbBr<sub>3</sub> NPLs is mainly due to the prolonged carrier lifetime and suppressed charge recombination due to the enhanced spin-polarized photogenerated carriers. The mechanism is further systematically explored by magnetic circular dichroism (MCD) spectroscopy, ultrafast transient absorption (TA) spectroscopy, and density functional theory (DFT) simulations. Our result shows that manipulating spin-polarized electrons in semiconductors doped with magnetic elements provides an effective strategy to boost photocatalytic  $\text{CO}_2$  reduction efficiencies.

## ■ RESULTS AND DISCUSSION

To obtain spin-polarized electrons in halide perovskite NPLs, the magnetic Mn<sup>2+</sup> ions are designed to embed into the three-dimensional (3D) all-inorganic perovskite  $\text{CsPbBr}_3$  NPLs, as shown in Figure 1a. These pristine  $\text{CsPbBr}_3$  and Mn-CsPbBr<sub>3</sub> NPLs were synthesized via the traditional hot-injection method.<sup>45,46</sup> The detailed synthesis method is described in the Supporting Information (SI). The structural morphology of both  $\text{CsPbBr}_3$  and Mn-CsPbBr<sub>3</sub> NPLs is investigated by transmission electron microscopy (TEM) and high-resolution transmission electron microscopy (HR-TEM), as shown in Figure 1b,c. The TEM morphological images in Figure 1b,c show that both  $\text{CsPbBr}_3$  and Mn-CsPbBr<sub>3</sub> NPLs have a rectangular shape with an average size of around 45 nm. HR-TEM images corresponding to the (101) Miller plane of the 3D perovskite orthorhombic phase are shown in the inset of Figure 1b,c.<sup>47</sup> The observed interplanar spacing for the (101) plane of  $\text{CsPbBr}_3$  and Mn-CsPbBr<sub>3</sub> NPLs was 0.43 and 0.41 nm, respectively. The thickness of both  $\text{CsPbBr}_3$  and Mn-CsPbBr<sub>3</sub> NPLs was approximately 3 nm, as measured by atomic force microscopy (AFM) in Figure S1. Moreover, high-angle annular dark-field scanning transmission microscopy (HAADF-STEM) equipped with energy-dispersive X-ray spectroscopy (EDS) element mapping was applied to gain more insight into the incorporation of Mn<sup>2+</sup> ion doping in Mn-CsPbBr<sub>3</sub> NPLs. Figure 1d shows the HAADF-STEM image of Mn-CsPbBr<sub>3</sub> NPLs and the corresponding EDS element mapping images of Cs, Pb, Br, and Mn. The Mn ions are homogeneously distributed among the Mn-CsPbBr<sub>3</sub> NPLs, as shown in the EDS mapping image of Mn (green dots). Furthermore, the quantitative Mn-doping ratio of Mn-CsPbBr<sub>3</sub> NPLs was approximately 3.2 mol %, as measured by inductively coupled plasma mass spectrometry (ICP-MS). The crystal structures of both  $\text{CsPbBr}_3$  and Mn-CsPbBr<sub>3</sub> NPLs are measured by powder X-ray diffraction (PXRD) measurements, as shown in Figure 1e. The PXRD patterns of both  $\text{CsPbBr}_3$  and Mn-CsPbBr<sub>3</sub> NPLs belong to the 3D perovskite orthorhombic phase, which echoes the aforementioned HR-TEM results and recent work.<sup>47,48</sup> In particular, the PXRD patterns of Mn-CsPbBr<sub>3</sub> NPLs shift to a higher angle direction compared to the host  $\text{CsPbBr}_3$  NPLs because of the substitution of the larger lead ion (ionic radius of Pb<sup>2+</sup> is 1.33 Å) in the octahedral unit with the smaller manganese ion (ionic radius of Mn<sup>2+</sup> is 0.97 Å) and the occupation of the interstitial sites, which result in lattice contraction.<sup>46,48,49</sup> The observed shift in the angle is around 0.2°. The occupation of the interstitial sites can tailor the local crystal field, which is expected to tailor their radiation parameters and affect their anti-Stokes luminescence.<sup>49</sup> The valence and spin states of magnetic Mn ion doping into  $\text{CsPbBr}_3$  NPLs were further

confirmed by Mn L<sub>3,2</sub>-edge X-ray absorption near-edge structure (XANES) spectroscopy. Figure 1f shows that the normalized Mn L<sub>3,2</sub>-edge XANES spectra of Mn-CsPbBr<sub>3</sub> matched the published MnO reference results, suggesting that the magnetic Mn ions in Mn-CsPbBr<sub>3</sub> NPLs are high-spin-state Mn<sup>2+</sup> ions.<sup>50,51</sup> These results indicate that the magnetic Mn<sup>2+</sup> ions were successfully doped into the all-inorganic halide perovskite  $\text{CsPbBr}_3$  NPLs.

Figure 2a,b shows the absorption and photoluminescence (PL) spectra of  $\text{CsPbBr}_3$  and Mn-CsPbBr<sub>3</sub> NPLs. The absorption of  $\text{CsPbBr}_3$  and Mn-CsPbBr<sub>3</sub> NPLs shows sharp excitonic absorption peaks at around 415 and 405 nm, respectively, which are clearly blue-shifted compared to the absorption peak of the conventional 3D  $\text{CsPbBr}_3$  perovskite nanocube (500 nm).<sup>45</sup> Accordingly, the obvious blue shift of 85 and 95 nm in the absorption spectra for  $\text{CsPbBr}_3$  NPLs and Mn-CsPbBr<sub>3</sub> NPLs, respectively, compared to the conventional 3D  $\text{CsPbBr}_3$  perovskite nanocube originates from the quantum size effect due to the thin  $\text{CsPbBr}_3$  and Mn-CsPbBr<sub>3</sub> NPLs (the thickness is about 3 nm from Figure S1).<sup>52</sup> The corresponding PL spectra of  $\text{CsPbBr}_3$  NPLs and Mn-CsPbBr<sub>3</sub> NPLs exhibited an excitonic emission peak position at 430 and 435 nm, respectively. Unlike  $\text{CsPbBr}_3$  NPLs, an additional emission peak in the PL spectra is observed for Mn-CsPbBr<sub>3</sub> NPLs at around 600 nm due to the magnetic Mn<sup>2+</sup> ions inducing a strong sp–d exchange interaction, which confirms the successful incorporation of Mn<sup>2+</sup> into  $\text{CsPbBr}_3$  NPLs.<sup>47,53</sup> The incorporation of Mn<sup>2+</sup> ion doping in  $\text{CsPbBr}_3$  NPLs not only modifies their structural and optoelectronic properties but also induces spin polarization. Figure 2c shows the electron paramagnetic resonance (EPR) spectrum of Mn-CsPbBr<sub>3</sub> NPLs. The EPR spectrum of Mn-CsPbBr<sub>3</sub> NPLs exhibits a strong signal at approximately 3300 Gauss (corresponding to a g-factor of around 2) with six hyperfine splittings originating from the interaction between the magnetic Mn<sup>2+</sup> ion nuclear spin ( $S = 5/2$ ) and its electron spin.<sup>54</sup> By contrast, no EPR signal is observed for  $\text{CsPbBr}_3$  NPLs. The feature of these broad six hyperfine splittings reveals that the magnetic Mn<sup>2+</sup> ions also change the local structures of Mn-CsPbBr<sub>3</sub>, resulting from a dipolar interaction.<sup>55</sup> Figure 2d shows the spin-polarized density of state (DOS) of Mn-CsPbBr<sub>3</sub> calculated by DFT simulation, where the difference in the DOSs of the spin-up and spin-down electrons around the Fermi level is calculated. The spin-polarized DOSs of both the valence band (VB) and conduction band (CB) of Mn-CsPbBr<sub>3</sub> originate from the doping magnetic Mn<sup>2+</sup> ions. By contrast, no spin-polarized DOS is observed for the pristine  $\text{CsPbBr}_3$  (Figure S3). The real-space charge distribution of the Mn-CsPbBr<sub>3</sub> is shown in the inset of Figure 2d, where a more localized character in proximity to the central Mn atom is observed. The result indicates that spin-polarized electrons are introduced by doping with the magnetic element Mn in the perovskite  $\text{CsPbBr}_3$  NPLs.

Next, we examine the effect of enhanced spin-polarized electrons on the photocatalytic  $\text{CO}_2$ RR of  $\text{CsPbBr}_3$  and Mn-CsPbBr<sub>3</sub> NPLs. The photocatalytic  $\text{CO}_2$ RR was demonstrated by placing  $\text{CsPbBr}_3$  and Mn-CsPbBr<sub>3</sub> NPLs within  $\text{CO}_2$ -saturated water vapor under simulated solar irradiation AM 1.5G (100 mW cm<sup>-2</sup>), as shown in Figure S4. The detailed photocatalytic experiments are described in SI. Figure 2e shows that the main products of  $\text{CsPbBr}_3$  and Mn-CsPbBr<sub>3</sub> NPLs for photocatalytic  $\text{CO}_2$ RR are CO and CH<sub>4</sub>, respectively. The concentration of both CO and CH<sub>4</sub> increased

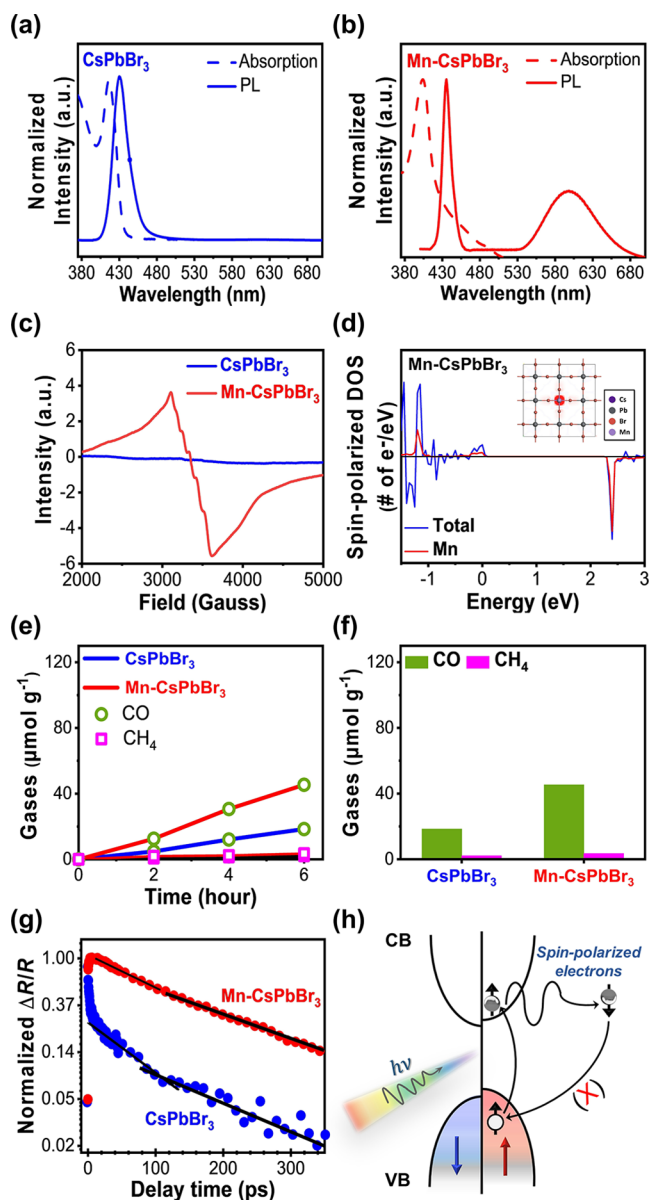


**Figure 2.** Optical properties, spin-polarized properties, and the photocatalytic performance of CsPbBr<sub>3</sub> and Mn-CsPbBr<sub>3</sub> NPLs. The UV-vis absorption and PL spectroscopy of (a) CsPbBr<sub>3</sub> and (b) Mn-CsPbBr<sub>3</sub> NPLs. (c) EPR spectroscopy of CsPbBr<sub>3</sub> (blue) and Mn-CsPbBr<sub>3</sub> (red) NPLs. (d) Spin-polarized DOS of Mn-CsPbBr<sub>3</sub> NPLs. The inset is the real-space charge distribution of Mn-CsPbBr<sub>3</sub> NPLs. (e) Product yields of CO and CH<sub>4</sub> gases over CsPbBr<sub>3</sub> and Mn-CsPbBr<sub>3</sub> NPLs during 6 h under AM 1.5 simulated solar irradiation. (f) The photocatalytic CO<sub>2</sub>RR product yields of CsPbBr<sub>3</sub> and Mn-CsPbBr<sub>3</sub> NPLs after 6 h. (g) The normalized photoinduced transient reflectivity changes ( $\Delta R/R$ ) of CsPbBr<sub>3</sub> and Mn-CsPbBr<sub>3</sub> NPLs. (h) Schematic illustration of the electron spin polarization suppressed the carrier recombination of Mn-CsPbBr<sub>3</sub> NPLs.

linearly during the 6 h (Figure S7). In addition, two control experiments (without light illumination and in a N<sub>2</sub> atmosphere) and <sup>13</sup>CO<sub>2</sub> isotopic labeling experiments were performed. The results demonstrate that the products generated from photocatalytic CO<sub>2</sub>RR over CsPbBr<sub>3</sub> NPLs originated from CO<sub>2</sub> rather than surface ligands, as shown in Figure S8. As shown in Figure 2f, the product yields of CO and CH<sub>4</sub> over the pristine CsPbBr<sub>3</sub> NPLs are 18.4 and 2.1  $\mu\text{mol g}^{-1}$ , respectively, which are comparable with the reported

product yields of CsPbBr<sub>3</sub> nanocrystals,<sup>18,22,24,56–58</sup> as shown in Table S1. By contrast, the corresponding product yields of CO and CH<sub>4</sub> over Mn-CsPbBr<sub>3</sub> NPLs are 45.4 and 3.5  $\mu\text{mol g}^{-1}$ , respectively, which are remarkably higher than the product yields over the pristine CsPbBr<sub>3</sub> NPLs. The Mn-CsPbBr<sub>3</sub> NPLs exhibit a higher photocatalytic activity for the CO<sub>2</sub> reduction reaction compared to the pristine CsPbBr<sub>3</sub> NPLs, mainly resulting from the presence of spin-polarized electrons induced by the doping of magnetic Mn<sup>2+</sup> ions. To further investigate the corresponding carrier dynamics of CsPbBr<sub>3</sub> and Mn-CsPbBr<sub>3</sub> NPLs, we applied an ultrafast pump-probe measurement. As shown in Figure 2g, the photoinduced transient reflectivity changes ( $\Delta R/R$ ) reveal that the photo-excited electrons in the CB release their energy through the intraband electron-electron scattering and the excitons decay via the phonon-assisted nonradiative recombination.<sup>59</sup> As a result, a prolonged nonradiative recombination lifetime can be observed for the Mn-CsPbBr<sub>3</sub> NPLs ( $\tau_1$ : 54.5 ps and  $\tau_2$ : 261.5 ps) compared to the pristine CsPbBr<sub>3</sub> NPLs ( $\tau_1$ : 10.9 ps and  $\tau_2$ : 135.9 ps; more details in the SI) because of the suppression of the carrier recombination rate due to the presence of spin polarization electrons. The experimental observation can be further explained by the mechanism of quantum spin exchange interactions (QSEIs), as reported in studies.<sup>60–63</sup> QSEI can stabilize open-shell orbital configurations with unpaired electrons in magnetic compositions, which are important in catalysts with configurations consisting of unpaired electrons. Doping of high-spin magnetic Mn<sup>2+</sup> ions (with 3d orbitals) in the perovskite semiconductors leads to the presence of spin-polarized electrons and nonsymmetric DOS, as shown in Figure 2h. By contrast, the pristine CsPbBr<sub>3</sub> NPLs with symmetric DOS lack spin-polarized electrons, as seen in Figure S3. After light illumination, the spin-polarized electrons of Mn-CsPbBr<sub>3</sub> NPLs are excited to the CB, while the spin-polarized holes with the same spin direction remain in the valence band (VB). The presence of QSEI increases the exchange of electron spin delocalization and decreases the repulsion of the electrons, leading to the spin-correlated unpaired electrons being more stable at the energy states.<sup>60</sup> Therefore, the QSEI can efficiently make the electrons with the same spin direction to transport easily.<sup>60</sup> Meanwhile, the photoexcited spin-polarized electrons in the CB are likely to undergo spin relaxation (or spin-flip) and lose their original spin direction during the charge-transfer process due to the strong spin-orbital coupling and hyperfine interaction.<sup>35,36</sup> The strong spin-orbital coupling of Mn-CsPbBr<sub>3</sub> NPLs mainly originated from the quantum confinement effect and heavy Pb<sup>2+</sup> atoms.<sup>44,64</sup> Accordingly, the carrier recombination rate is largely suppressed because of the lack of spin-polarized holes with the same spin direction in the VB. This may lead to a longer carrier lifetime of Mn-doped CsPbBr<sub>3</sub> compared to that of the pristine CsPbBr<sub>3</sub>. On the other hand, the doping of high-spin magnetic Mn<sup>2+</sup> ions in CsPbBr<sub>3</sub> can also affect the photocatalytic oxygen evolution reaction (OER) due to the presence of QSEI.<sup>60,62,63</sup> The QSEI can help to stabilize the antibonding 3d orbitals and accumulate the spin-polarized holes for bonding with oxygen molecules, leading to enhanced photocatalytic OER activity as compared to the pristine CsPbBr<sub>3</sub>.<sup>62</sup> Therefore, the presence of spin-polarized electrons induced by the doping of magnetic Mn<sup>2+</sup> ions in CsPbBr<sub>3</sub> NPLs may effectively facilitate the redox reactions for the photocatalytic CO<sub>2</sub>RR compared to the pristine CsPbBr<sub>3</sub> NPLs.

Moreover, it is well known that the electron spin polarization in semiconductors can be further enhanced by applying an external magnetic field.<sup>35,36,65,66</sup> Here, an external magnetic field of up to 300 mT is applied to further enhance the photocatalytic performance of Mn-CsPbBr<sub>3</sub> NPLs. A permanent magnet that requires no extra power supply is used as the source of the external magnetic field. The experimental setup of the photocatalytic CO<sub>2</sub>RR with permanent magnets is shown in Figures S4 and S5. Figure 3a,b shows the evolution of

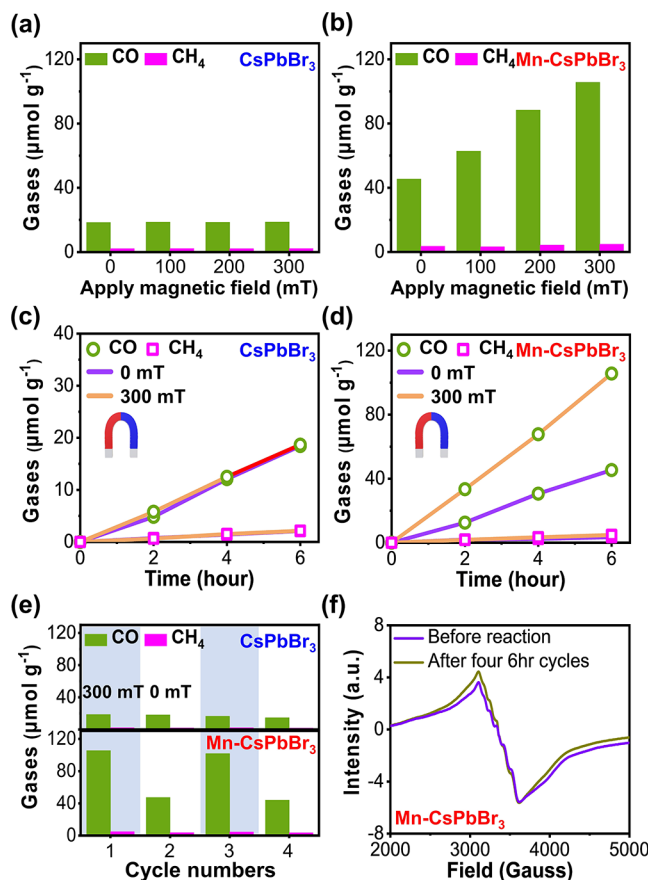


**Figure 3.** Photocatalytic performance of CsPbBr<sub>3</sub> and Mn-CsPbBr<sub>3</sub> NPLs with and without an external magnetic field. The photocatalytic CO<sub>2</sub>RR product yields of (a) CsPbBr<sub>3</sub> and (b) Mn-CsPbBr<sub>3</sub> NPLs under different external magnetic fields (from 0 to 300 mT) after 6 h of light illumination. Product yields of CO and CH<sub>4</sub> gases over (c) CsPbBr<sub>3</sub> and (d) Mn-CsPbBr<sub>3</sub> NPLs with and without an external magnetic field (0 and 300 mT) during 6 h under light irradiation. (e) The photocatalytic stability test of CsPbBr<sub>3</sub> (up) and Mn-CsPbBr<sub>3</sub> (down) NPLs with and without an external magnetic field (0 and 300 mT) for four 6 h cycles. (f) EPR spectroscopy of Mn-CsPbBr<sub>3</sub> NPLs before and after four 6 h cycles of the photocatalytic CO<sub>2</sub>RR.

the photocatalytic CO<sub>2</sub>RR of pristine CsPbBr<sub>3</sub> and Mn-CsPbBr<sub>3</sub> NPLs under an external magnetic field ranging from 0 to 300 mT. For the pristine CsPbBr<sub>3</sub> NPLs, the product yields of both CO and CH<sub>4</sub> are unaltered with the increase of the external magnetic field from 0 to 300 mT. By contrast, the enhancement of the photocatalytic performance over Mn-CsPbBr<sub>3</sub> NPLs highly correlates with the increase of the external magnetic field from 0 to 300 mT. The evolution of the product yields of both CO and CH<sub>4</sub> for the pristine CsPbBr<sub>3</sub> NPLs and Mn-CsPbBr<sub>3</sub> NPLs with and without a magnetic

field is shown in Figure 3c,d, respectively. The product yield of CO over Mn-CsPbBr<sub>3</sub> NPLs under 300 mT (105.7 μmol g<sup>-1</sup>) is 2.3 times larger than that under 0 mT (45.4 μmol g<sup>-1</sup>), while the product yield of CH<sub>4</sub> under 300 mT (4.8 μmol g<sup>-1</sup>) is 1.6 times larger than that under 0 mT (3.5 μmol g<sup>-1</sup>), as shown in Figure 3d. The results indicate that the photocatalytic CO<sub>2</sub>RR performance of Mn-CsPbBr<sub>3</sub> NPLs can be further enhanced by applying an external magnetic field. By contrast, no such correlation is found over the pristine CsPbBr<sub>3</sub> NPLs. Figure 3e shows the superior photocatalytic stability and reproducibility of Mn-CsPbBr<sub>3</sub> NPLs with the product yields of both CO and CH<sub>4</sub> after four consecutive cycles with and without an external magnetic field (0 and 300 mT). Figure 3f also shows that the EPR signature of the spin-polarized properties of Mn-CsPbBr<sub>3</sub> NPLs is almost unchanged after four 6 h cycles. The result suggests that the excellent stability of the photocatalytic performance of Mn-CsPbBr<sub>3</sub> NPLs can be achieved by applying an external magnetic field over 24 h.

The above results indicate that the photocatalytic CO<sub>2</sub>RR efficiencies of Mn-CsPbBr<sub>3</sub> NPLs greatly correlate with the electron spin polarization. We performed MCD spectroscopy and ultrafast TA spectroscopy under a magnetic field to further examine the origin of the magnetic field-enhanced photocatalytic CO<sub>2</sub>RR over Mn-CsPbBr<sub>3</sub> NPLs. MCD is the difference in absorption between the left circular polarized ( $A_{LCP}$ ) and right circular polarized ( $A_{RCP}$ ) lights as the linearly polarized light is transmitted to a medium under a magnetic field, originating from the splitting of states by the Zeeman splitting energy  $\Delta E_Z$ . The presence of the MCD signal indicates the existence of a spin-polarized band structure. Figure 4a,b shows the MCD spectra of pristine CsPbBr<sub>3</sub> and

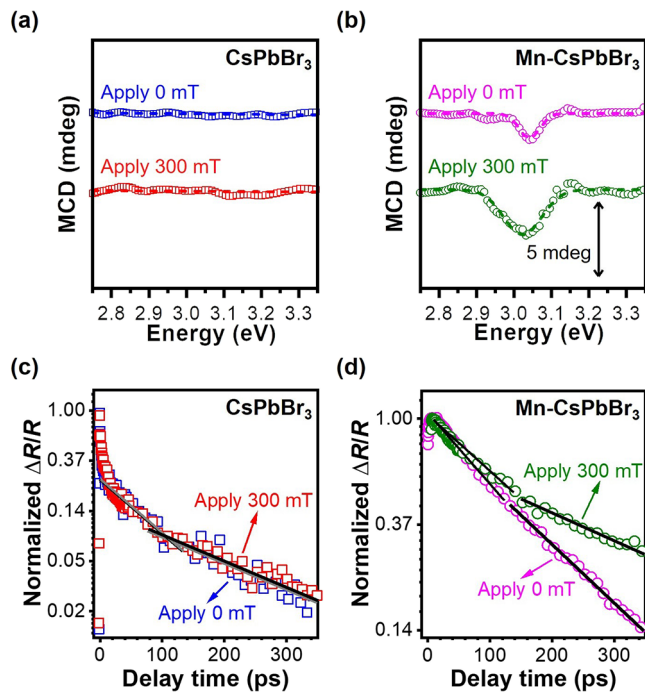


**Figure 4.** MCD spectroscopy and ultrafast carrier dynamics of CsPbBr<sub>3</sub> and Mn-CsPbBr<sub>3</sub> NPLs with and without an external magnetic field. The MCD spectroscopy of (a) CsPbBr<sub>3</sub> and (b) Mn-CsPbBr<sub>3</sub> NPLs with and without an external magnetic field (0 and 300 mT). The normalized photoinduced transient reflectivity changes ( $\Delta R/R$ ) of (c) CsPbBr<sub>3</sub> and (d) Mn-CsPbBr<sub>3</sub> NPLs with and without an external magnetic field (0 and 300 mT).

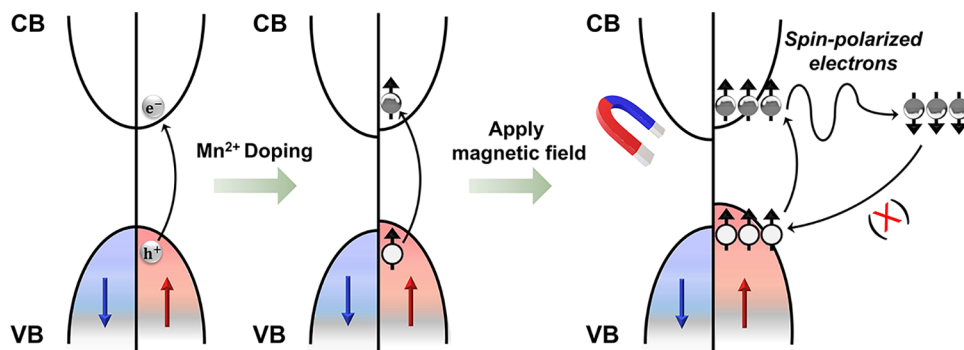


**Figure 5.** Schematic illustration of the electron spin polarization induced a longer photoexcited carrier lifetime under an external magnetic field in Mn-CsPbBr<sub>3</sub> NPLs.

Mn-CsPbBr<sub>3</sub> NPLs under 0 and 300 mT, respectively. No detectable MCD signal is observed for the pristine CsPbBr<sub>3</sub> with and without a magnetic field. By contrast, the presence of an MCD signal at the Mn-CsPbBr<sub>3</sub> NPLs without a magnetic field (0 mT) indicates an intrinsic spin-polarized band structure. Because the energy position of the MCD peak is close to the energy gap of the Mn-CsPbBr<sub>3</sub> NPLs, the origin of the MCD signal is attributed to the intrinsic spin-polarized band splitting near the band edges due to the doping of magnetic Mn<sup>2+</sup> ions. When a magnetic field was applied, the magnitude of the band splitting in Mn-CsPbBr<sub>3</sub> NPLs is increased due to the Zeeman effect, leading to an enhanced MCD signal. The result indicates that the spin polarization of the photoexcited carriers of Mn-CsPbBr<sub>3</sub> NPLs can be significantly enhanced under an external magnetic field. The corresponding carrier dynamics of CsPbBr<sub>3</sub> and Mn-CsPbBr<sub>3</sub> NPLs with and without an external magnetic field were further verified by the ultrafast pump–probe measurement under an external magnetic field. Figure 4c,d shows the transient reflectivity changes  $\Delta R/R$  decay curves of CsPbBr<sub>3</sub> and Mn-CsPbBr<sub>3</sub> NPLs with and without an external magnetic field, respectively. Mn-CsPbBr<sub>3</sub> NPLs exhibit both biexciton ( $\tau_1$ ) and single exciton ( $\tau_2$ ) decays with a prolonged relaxation lifetime from  $\tau_1 = 54.5$  ps and  $\tau_2 = 261.5$  ps (0 mT) to  $\tau_1 = 93.0$  ps and  $\tau_2 = 369.5$  ps (300 mT), respectively, as a result of the suppressed phonon-assisted nonradiative recombination rates. By contrast, there is no change in the transient reflectivity changes  $\Delta R/R$  decay curves of pristine CsPbBr<sub>3</sub> NPLs with and without an external magnetic field. The enhanced electron spin polarization of Mn-CsPbBr<sub>3</sub> NPLs under an external magnetic field results in a prolonged lifetime of the photogenerated charge carriers, which significantly reduces the carrier recombination. This may enhance the diffusion of the photogenerated carriers to the surface to facilitate the redox reactions for the photocatalytic CO<sub>2</sub>RR. Figure 5 summarizes the correlation between manipulating the spin polarization of Mn-CsPbBr<sub>3</sub> NPLs and enhancing the photocatalytic CO<sub>2</sub>RR. First, the spin-polarized bands in both the VB and CB are obtained by doping the magnetic Mn<sup>2+</sup> ions into the perovskite CsPbBr<sub>3</sub> NPLs. Under light illumination, the spin-polarized electrons in Mn-CsPbBr<sub>3</sub> NPLs result in a longer carrier lifetime and a slower recombination rate compared to those in the pristine CsPbBr<sub>3</sub> NPLs. Meanwhile, the enhanced spin-polarized holes in VB may also facilitate the oxidation reaction process. This explains the enhanced performance of the photocatalytic CO<sub>2</sub>RR in Mn-CsPbBr<sub>3</sub> NPLs compared to that in the pristine CsPbBr<sub>3</sub> NPLs. After an

external magnetic field is applied, the enhanced splitting of the spin-polarized bands in Mn-CsPbBr<sub>3</sub> NPLs due to the Zeeman effect leads to the further increase of spin-polarized electrons and holes. This may further suppress the carrier recombination rate and facilitate the overall redox reactions for the photocatalytic CO<sub>2</sub>RR, contributing to the improved photocatalytic performance. The above mechanism indicates that manipulating the spin polarization in Mn-CsPbBr<sub>3</sub> NPLs by doping magnetic Mn<sup>2+</sup> ions or applying a magnetic field is an effective strategy to boost the photocatalytic CO<sub>2</sub> reduction efficiencies.

## CONCLUSIONS

In summary, we designed and synthesized spin-polarized halide perovskite NPLs via doping magnetic Mn<sup>2+</sup> ions in all-inorganic CsPbBr<sub>3</sub> perovskite NPLs. With synergistic doping of the magnetic elements and applying a magnetic field, the photocatalytic CO<sub>2</sub> reduction efficiencies of Mn-CsPbBr<sub>3</sub> NPLs are largely improved compared to those of the pristine CsPbBr<sub>3</sub> NPLs. It results from the significantly suppressed carrier recombination rates due to the enhanced spin polarization of Mn-CsPbBr<sub>3</sub> NPLs. It is worth noting that such considerably enhanced photocatalytic CO<sub>2</sub> reduction efficiencies of Mn-CsPbBr<sub>3</sub> NPLs can be achieved by simply applying a permanent magnet without additional power consumption, which works as a promising and feasible approach as considering in the future application of solar to fuel conversion.

## ASSOCIATED CONTENT

### Supporting Information

The Supporting Information is available free of charge at <https://pubs.acs.org/doi/10.1021/jacs.2c06060>.

Experimental section, AFM data, band gaps of perovskite NPLs, spin-polarized DOS of the pristine CsPbBr<sub>3</sub>, setup of photocatalytic CO<sub>2</sub>RR, calibration curves of CO and CH<sub>4</sub>, evolutions of products over perovskite NPLs under different external magnetic fields, control experiments and <sup>13</sup>CO<sub>2</sub> isotopic experiment, comparison of photocatalytic CO<sub>2</sub>RR conversion efficiencies, decay times of perovskite NPLs, and setup of MCD measurements (PDF)

## AUTHOR INFORMATION

### Corresponding Authors

**Chia-Chun Chen** — Department of Chemistry, National Taiwan Normal University, Taipei 11677, Taiwan; Institute of Atomic and Molecular Sciences, Academia Sinica, Taipei 10617, Taiwan; [orcid.org/0000-0001-6491-0482](https://orcid.org/0000-0001-6491-0482); Email: [cjchen@ntnu.edu.tw](mailto:cjchen@ntnu.edu.tw)

**Chun-Wei Chen** — International Graduate Program of Molecular Science and Technology, National Taiwan University (NTU-MST), Taipei 10617, Taiwan; Department of Materials Science and Engineering and Center for Condensed Matter Sciences, National Taiwan University, Taipei 10617, Taiwan; Center of Atomic Initiative for New Materials (AI-MAT), National Taiwan University (NTU), Taipei 10617, Taiwan; [orcid.org/0000-0003-3096-249X](https://orcid.org/0000-0003-3096-249X); Email: [chunwei@ntu.edu.tw](mailto:chunwei@ntu.edu.tw)

### Authors

**Cheng-Chieh Lin** — International Graduate Program of Molecular Science and Technology, National Taiwan University (NTU-MST), Taipei 10617, Taiwan; Molecular Science and Technology Program, Taiwan International Graduate Program (TIGP), Academia Sinica, Taipei 11529, Taiwan; [orcid.org/0000-0003-1895-493X](https://orcid.org/0000-0003-1895-493X)

**Ting-Ran Liu** — Department of Materials Science and Engineering, National Taiwan University, Taipei 10617, Taiwan

**Sin-Rong Lin** — Department of Chemistry, National Taiwan Normal University, Taipei 11677, Taiwan

**Karunakara Moorthy Boopathi** — Department of Materials Science and Engineering, National Taiwan University, Taipei 10617, Taiwan; [orcid.org/0000-0003-2042-9595](https://orcid.org/0000-0003-2042-9595)

**Chun-Hao Chiang** — Department of Materials Science and Engineering, National Taiwan University, Taipei 10617, Taiwan; [orcid.org/0000-0002-9066-4657](https://orcid.org/0000-0002-9066-4657)

**Wen-Yen Tzeng** — Department of Electrophysics, National Yang Ming Chiao Tung University, Hsinchu 30010, Taiwan

**Wan-Hsiu Chang Chien** — Department of Applied Physics, National Pingtung University, Pingtung 90044, Taiwan

**Hua-Shu Hsu** — Department of Applied Physics, National Pingtung University, Pingtung 90044, Taiwan; [orcid.org/0000-0002-5773-2451](https://orcid.org/0000-0002-5773-2451)

**Chih-Wei Luo** — Department of Electrophysics, National Yang Ming Chiao Tung University, Hsinchu 30010, Taiwan; Institute of Physics and Center for Emergent Functional Matter Science, National Yang Ming Chiao Tung University, Hsinchu 30010, Taiwan; National Synchrotron Radiation Research Center, Hsinchu 30076, Taiwan; Taiwan Consortium of Emergent Crystalline Materials (TCECM), Ministry of Science and Technology, Taipei 10622, Taiwan; [orcid.org/0000-0002-6453-7435](https://orcid.org/0000-0002-6453-7435)

**Hui-Ying Tsai** — Department of Chemistry, National Taiwan Normal University, Taipei 11677, Taiwan

**Hsin-An Chen** — Institute of Materials Science and Engineering, National Taipei University of Technology, Taipei 10608, Taiwan

**Pai-Chia Kuo** — Institute of Atomic and Molecular Sciences, Academia Sinica, Taipei 10617, Taiwan

**Jessie Shiue** — Institute of Atomic and Molecular Sciences, Academia Sinica, Taipei 10617, Taiwan; Institute of Physics, Academia Sinica, Taipei 11520, Taiwan

**Jau-Wern Chiou** — Department of Applied Physics, National University of Kaohsiung, Kaohsiung 81148, Taiwan

**Way-Faung Pong** — Department of Physics, Tamkang University, New Taipei City 25137, Taiwan

Complete contact information is available at:  
<https://pubs.acs.org/10.1021/jacs.2c06060>

### Notes

The authors declare no competing financial interest.

## ACKNOWLEDGMENTS

C.-W.C. acknowledges the financial support from the Ministry of Science and Technology (MOST), Taiwan (Grant No. 108-2923-M-002-002-MY2, MOST-NIMS add-on project), and the Taiwan Consortium of Emergent Crystalline Materials (TCECM). C.-C.C. acknowledges the financial support from the Ministry of Science and Technology (MOST), Taiwan (Project Nos. 108-2119-M-003-001 and 109-2113-M-003-011-MY3). In addition, financial support by the Center of Atomic Initiative for New Materials (AI-MAT), National Taiwan University, from the Featured Areas Research Center Program within the framework of the Higher Education Sprout Project by the Ministry of Education in Taiwan (108L9008) is acknowledged. The XANES spectra obtained from Taiwan Photon Source (TPS) 45A2 beamline at the National Synchrotron Radiation Research Center (NSRRC) are appreciated. In addition, technical support from the Advanced Materials Characterization lab at Academia Sinica is acknowledged.

## REFERENCES

- (1) Low, J.; Cheng, B.; Yu, J. Surface Modification and Enhanced Photocatalytic CO<sub>2</sub> Reduction Performance of TiO<sub>2</sub>: A Review. *Appl. Surf. Sci.* **2017**, *392*, 658–686.
- (2) Albero, J.; Peng, Y.; García, H. Photocatalytic CO<sub>2</sub> Reduction to C<sub>2+</sub> Products. *ACS Catal.* **2020**, *10*, 5734–5749.
- (3) Wagner, A.; Sahm, C. D.; Reisner, E. Towards Molecular Understanding of Local Chemical Environment Effects in Electro- and Photocatalytic CO<sub>2</sub> Reduction. *Nat. Catal.* **2020**, *3*, 775–786.
- (4) Gong, Y.-N.; Zhong, W.; Li, Y.; Qiu, Y.; Zheng, L.; Jiang, J.; Jiang, H.-L. Regulating Photocatalysis by Spin-State Manipulation of Cobalt in Covalent Organic Frameworks. *J. Am. Chem. Soc.* **2020**, *142*, 16723–16731.
- (5) Ola, O.; Maroto-Valer, M. M. Review of Material Design and Reactor Engineering on TiO<sub>2</sub> Photocatalysis for CO<sub>2</sub> Reduction. *J. Photochem. Photobiol. C* **2015**, *24*, 16–42.
- (6) Li, K.; Peng, B.; Peng, T. Recent Advances in Heterogeneous Photocatalytic CO<sub>2</sub> Conversion to Solar Fuels. *ACS Catal.* **2016**, *6*, 7485–7527.
- (7) Chang, X.; Wang, T.; Gong, J. CO<sub>2</sub> Photo-Reduction: Insights into CO<sub>2</sub> Activation and Reaction on Surfaces of Photocatalysts. *Energy Environ. Sci.* **2016**, *9*, 2177–2196.
- (8) Wu, J.; Huang, Y.; Ye, W.; Li, Y. CO<sub>2</sub> Reduction: From the Electrochemical to Photochemical Approach. *Adv. Sci.* **2017**, *4*, No. 1700194.
- (9) Fresno, F.; Villar-Garcia, I. J.; Collado, L.; Alfonso-Gonzalez, E.; Renones, P.; Barawi, M.; de la Pena O'Shea, V. A. Mechanistic View of the Main Current Issues in Photocatalytic CO<sub>2</sub> Reduction. *J. Phys. Chem. Lett.* **2018**, *9*, 7192–7204.
- (10) Saidaminov, M. I.; Williams, K.; Wei, M.; Johnston, A.; Quintero-Bermudez, R.; Vafaei, M.; Pina, J. M.; Proppe, A. H.; Hou, Y.; Walters, G.; Kelley, S. O.; Tisdale, W. A.; Sargent, E. H. Multi-Cation Perovskites Prevent Carrier Reflection from Grain Surfaces. *Nat. Mater.* **2020**, *19*, 412–418.
- (11) Zhang, L.; Yang, X.; Jiang, Q.; Wang, P.; Yin, Z.; Zhang, X.; Tan, H.; Yang, Y. M.; Wei, M.; Sutherland, B. R.; Sargent, E. H.; You, J. Ultra-Bright and Highly Efficient Inorganic Based Perovskite Light-Emitting Diodes. *Nat. Commun.* **2017**, *8*, No. 15640.

- (12) Dong, Q.; Fang, Y.; Shao, Y.; Mulligan, P.; Qiu, J.; Cao, L.; Huang, J. Electron-Hole Diffusion Lengths > 175  $\mu\text{m}$  in Solution-Grown  $\text{CH}_3\text{NH}_3\text{PbI}_3$  Single Crystals. *Science* **2015**, *347*, 967–970.
- (13) Park, N.-G.; Zhu, K. Scalable Fabrication and Coating Methods for Perovskite Solar Cells and Solar Modules. *Nat. Rev. Mater.* **2020**, *5*, 333–350.
- (14) Lin, C. C.; Huang, S. J.; Wu, P. H.; Chen, T. P.; Huang, C. Y.; Wang, Y. C.; Chen, P. T.; Radeva, D.; Petrov, O.; Gelev, V. M.; Sankar, R.; Chen, C. C.; Chen, C. W.; Yu, T. Y. Direct Investigation of the Reorientational Dynamics of A-Site Cations in 2D Organic-Inorganic Hybrid Perovskite by Solid-State NMR. *Nat. Commun.* **2022**, *13*, No. 1513.
- (15) Lin, C. C.; Li, J. Y.; She, N. Z.; Huang, S. K.; Huang, C. Y.; Wang, I. T.; Tsai, F. L.; Wei, C. Y.; Lee, T. Y.; Wang, D. Y.; Wen, C. Y.; Li, S. S.; Yabushita, A.; Luo, C. W.; Chen, C. C.; Chen, C. W. Stabilized High-Membered and Phase-Pure 2D All Inorganic Ruddlesden-Popper Halide Perovskites Nanocrystals as Photocatalysts for the  $\text{CO}_2$  Reduction Reaction. *Small* **2022**, *18*, No. 2107881.
- (16) Xu, Y. F.; Yang, M. Z.; Chen, B. X.; Wang, X. D.; Chen, H. Y.; Kuang, D. B.; Su, C. Y. A  $\text{CsPbBr}_3$  Perovskite Quantum Dot/Graphene Oxide Composite for Photocatalytic  $\text{CO}_2$  Reduction. *J. Am. Chem. Soc.* **2017**, *139*, 5660–5663.
- (17) Huang, H.; Pradhan, B.; Hofkens, J.; Roeffaers, M. B. J.; Steele, J. A. Solar-Driven Metal Halide Perovskite Photocatalysis: Design, Stability, and Performance. *ACS Energy Lett.* **2020**, *5*, 1107–1123.
- (18) Jiang, Y.; Liao, J.-F.; Chen, H.-Y.; Zhang, H.-H.; Li, J.-Y.; Wang, X.-D.; Kuang, D.-B. All-Solid-State Z-Scheme  $\alpha\text{-Fe}_2\text{O}_3$ /Amine-RGO/ $\text{CsPbBr}_3$  Hybrids for Visible-Light-Driven Photocatalytic  $\text{CO}_2$  Reduction. *Chem* **2020**, *6*, 766–780.
- (19) Bhosale, S. S.; Kharade, A. K.; Jokar, E.; Fathi, A.; Chang, S. M.; Diau, E. W. Mechanism of Photocatalytic  $\text{CO}_2$  Reduction by Bismuth-Based Perovskite Nanocrystals at the Gas-Solid Interface. *J. Am. Chem. Soc.* **2019**, *141*, 20434–20442.
- (20) DuBose, J. T.; Kamat, P. V. Efficacy of Perovskite Photocatalysis: Challenges to Overcome. *ACS Energy Lett.* **2022**, *7*, 1994–2011.
- (21) Schanze, K. S.; Kamat, P. V.; Yang, P.; Bisquert, J. Progress in Perovskite Photocatalysis. *ACS Energy Lett.* **2020**, *5*, 2602–2604.
- (22) Jiang, Y.; Liao, J.-F.; Xu, Y.-F.; Chen, H.-Y.; Wang, X.-D.; Kuang, D.-B. Hierarchical  $\text{CsPbBr}_3$  Nanocrystal-Decorated  $\text{ZnO}$  Nanowire/Macroporous Graphene Hybrids for Enhancing Charge Separation and Photocatalytic  $\text{CO}_2$  Reduction. *J. Mater. Chem. A* **2019**, *7*, 13762–13769.
- (23) Wang, J.; Wang, J.; Li, N.; Du, X.; Ma, J.; He, C.; Li, Z. Direct Z-Scheme 0D/2D Heterojunction of  $\text{CsPbBr}_3$  Quantum Dots/ $\text{Bi}_2\text{WO}_6$  Nanosheets for Efficient Photocatalytic  $\text{CO}_2$  Reduction. *ACS Appl. Mater. Interfaces* **2020**, *12*, 31477–31485.
- (24) Kong, Z.-C.; Liao, J.-F.; Dong, Y.-J.; Xu, Y.-F.; Chen, H.-Y.; Kuang, D.-B.; Su, C.-Y. Core@Shell  $\text{CsPbBr}_3$ @Zeolitic Imidazolate Framework Nanocomposite for Efficient Photocatalytic  $\text{CO}_2$  Reduction. *ACS Energy Lett.* **2018**, *3*, 2656–2662.
- (25) Wang, X. D.; Huang, Y. H.; Liao, J. F.; Jiang, Y.; Zhou, L.; Zhang, X. Y.; Chen, H. Y.; Kuang, D. B. In Situ Construction of a  $\text{Cs}_2\text{SnI}_6$  Perovskite Nanocrystal/ $\text{SnS}_2$  Nanosheet Heterojunction with Boosted Interfacial Charge Transfer. *J. Am. Chem. Soc.* **2019**, *141*, 13434–13441.
- (26) Xu, F.; Meng, K.; Cheng, B.; Wang, S.; Xu, J.; Yu, J. Unique S-Scheme Heterojunctions in Self-Assembled  $\text{TiO}_2/\text{CsPbBr}_3$  Hybrids for  $\text{CO}_2$  Photoreduction. *Nat. Commun.* **2020**, *11*, No. 4613.
- (27) Sun, Y.; Sun, S.; Yang, H.; Xi, S.; Gracia, J.; Xu, Z. J. Spin-Related Electron Transfer and Orbital Interactions in Oxygen Electrocatalysis. *Adv. Mater.* **2020**, *32*, No. 2003297.
- (28) Yan, J.; Wang, Y.; Zhang, Y.; Xia, S.; Yu, J.; Ding, B. Direct Magnetic Reinforcement of Electrocatalytic ORR/OER with Electromagnetic Induction of Magnetic Catalysts. *Adv. Mater.* **2021**, *33*, No. 2007525.
- (29) Ren, X.; Wu, T.; Sun, Y.; Li, Y.; Xian, G.; Liu, X.; Shen, C.; Gracia, J.; Gao, H. J.; Yang, H.; Xu, Z. J. Spin-Polarized Oxygen Evolution Reaction under Magnetic Field. *Nat. Commun.* **2021**, *12*, No. 2608.
- (30) Chen, F.; Ma, Z.; Ye, L.; Ma, T.; Zhang, T.; Zhang, Y.; Huang, H. Macroscopic Spontaneous Polarization and Surface Oxygen Vacancies Collaboratively Boosting  $\text{CO}_2$  Photoreduction on  $\text{BiOIO}_3$  Single Crystals. *Adv. Mater.* **2020**, *32*, No. 1908350.
- (31) Wang, Y.; Xu, W.; Zhang, Y.; Wu, Y.; Wang, Z.; Fu, L.; Bai, F.; Zhou, B.; Wang, T.; Cheng, L.; Shi, J.; Liu, H.; Yang, R. Introducing Spin Polarization into Atomically Thin 2D Carbon Nitride Sheets for Greatly Extended Visible-Light Photocatalytic Water Splitting. *Nano Energy* **2021**, *83*, No. 105783.
- (32) Garcés-Pineda, F. A.; Blasco-Ahicart, M.; Nieto-Castro, D.; López, N.; Galán-Mascarós, J. R. Direct Magnetic Enhancement of Electrocatalytic Water Oxidation in Alkaline Media. *Nat. Energy* **2019**, *4*, 519–525.
- (33) Zhang, W.; Banerjee-Ghosh, K.; Tassinari, F.; Naaman, R. Enhanced Electrochemical Water Splitting with Chiral Molecule-Coated  $\text{Fe}_3\text{O}_4$  Nanoparticles. *ACS Energy Lett.* **2018**, *3*, 2308–2313.
- (34) Sun, Y.; Ren, X.; Sun, S.; Liu, Z.; Xi, S.; Xu, Z. J. Engineering High-Spin State Cobalt Cations in Spinel Zinc Cobalt Oxide for Spin Channel Propagation and Active Site Enhancement in Water Oxidation. *Angew. Chem., Int. Ed.* **2021**, *60*, 14536–14544.
- (35) Pan, L.; Ai, M.; Huang, C.; Yin, L.; Liu, X.; Zhang, R.; Wang, S.; Jiang, Z.; Zhang, X.; Zou, J. J.; Mi, W. Manipulating Spin Polarization of Titanium Dioxide for Efficient Photocatalysis. *Nat. Commun.* **2020**, *11*, No. 418.
- (36) Li, Y.; Wang, Z.; Wang, Y.; Kovács, A.; Foo, C.; Dunin-Borkowski, R. E.; Lu, Y.; Taylor, R. A.; Wu, C.; Tsang, S. C. E. Local Magnetic Spin Mismatch Promoting Photocatalytic Overall Water Splitting with Exceptional Solar-to-Hydrogen Efficiency. *Energy Environ. Sci.* **2022**, *15*, 265–277.
- (37) Zhao, Z.; Wang, D.; Gao, R.; Wen, G.; Feng, M.; Song, G.; Zhu, J.; Luo, D.; Tan, H.; Ge, X.; Zhang, W.; Zhang, Y.; Zheng, L.; Li, H.; Chen, Z. Magnetic-Field-Stimulated Efficient Photocatalytic  $\text{N}_2$  Fixation over Defective  $\text{BaTiO}_3$  Perovskites. *Angew. Chem., Int. Ed.* **2021**, *60*, 11910–11918.
- (38) Dogutan, D. K.; Nocera, D. G. Artificial Photosynthesis at Efficiencies Greatly Exceeding That of Natural Photosynthesis. *Acc. Chem. Res.* **2019**, *52*, 3143–3148.
- (39) Chakrabarti, S.; Holub, M. A.; Bhattacharya, P.; Mishima, T. D.; Santos, M. B.; Johnson, M. B.; Blom, D. A. Spin-Polarized Light-Emitting Diodes with Mn-Doped InAs Quantum Dot Nanomagnets as A Spin Aligner. *Nano Lett.* **2005**, *5*, 209–212.
- (40) Hao, S.; Zhou, G.; Wu, J.; Duan, W.; Gu, B.-L. Spin-Polarized Electron Emitter: Mn-Doped GaN Nanotubes and Their Arrays. *Phys. Rev. B* **2004**, *69*, No. 113403.
- (41) Torma, A. J.; Li, W.; Zhang, H.; Tu, Q.; Klepov, V. V.; Brennan, M. C.; McCleese, C. L.; Krzyaniak, M. D.; Wasielewski, M. R.; Katan, C.; Even, J.; Holt, M. V.; Grusenmeyer, T. A.; Jiang, J.; Pachter, R.; Kanatzidis, M. G.; Blanc, J. C.; Mohite, A. D. Interstitial Nature of  $\text{Mn}^{2+}$  Doping in 2D Perovskites. *ACS Nano* **2021**, *15*, 20550–20561.
- (42) Ohno, H. Properties of Ferromagnetic III–V Semiconductors. *J. Magn. Magn. Mater.* **1999**, *200*, 110–129.
- (43) Erwin, S. C.; Zu, L.; Haftel, M. I.; Efros, A. L.; Kennedy, T. A.; Norris, D. J. Doping Semiconductor Nanocrystals. *Nature* **2005**, *436*, 91–94.
- (44) Li, C.; Hsu, S. C.; Lin, J. X.; Chen, J. Y.; Chuang, K. C.; Chang, Y. P.; Hsu, H. S.; Chen, C. H.; Lin, T. S.; Liu, Y. H. Giant Zeeman Splitting for Monolayer Nanosheets at Room Temperature. *J. Am. Chem. Soc.* **2020**, *142*, 20616–20623.
- (45) Protesescu, L.; Yakunin, S.; Bodnarchuk, M. I.; Krieg, F.; Caputo, R.; Hendon, C. H.; Yang, R. X.; Walsh, A.; Kovalenko, M. V. Nanocrystals of Cesium Lead Halide Perovskites ( $\text{CsPbX}_3$ , X = Cl, Br, and I): Novel Optoelectronic Materials Showing Bright Emission with Wide Color Gamut. *Nano Lett.* **2015**, *15*, 3692–3696.
- (46) Parobek, D.; Dong, Y.; Qiao, T.; Son, D. H. Direct Hot-Injection Synthesis of Mn-Doped  $\text{CsPbBr}_3$  Nanocrystals. *Chem. Mater.* **2018**, *30*, 2939–2944.

- (47) Zhang, K.; Zhao, J.; Hu, Q.; Yang, S.; Zhu, X.; Zhang, Y.; Huang, R.; Ma, Y.; Wang, Z.; Ouyang, Z.; Han, J.; Han, Y.; Tang, J.; Tong, W.; Zhang, L.; Zhai, T. Room-Temperature Magnetic Field Effect on Excitonic Photoluminescence in Perovskite Nanocrystals. *Adv. Mater.* **2021**, *33*, No. 2008225.
- (48) Zou, S.; Liu, Y.; Li, J.; Liu, C.; Feng, R.; Jiang, F.; Li, Y.; Song, J.; Zeng, H.; Hong, M.; Chen, X. Stabilizing Cesium Lead Halide Perovskite Lattice through Mn(II) Substitution for Air-Stable Light-Emitting Diodes. *J. Am. Chem. Soc.* **2017**, *139*, 11443–11450.
- (49) Han, S.; Deng, R.; Xie, X.; Liu, X. Enhancing Luminescence in Lanthanide-Doped Upconversion Nanoparticles. *Angew. Chem., Int. Ed.* **2014**, *53*, 11702–11715.
- (50) Gilbert, B.; Frazer, B. H.; Belz, A.; Conrad, P. G.; Nealson, K. H.; Haskel, D.; Lang, J. C.; Srager, G.; De Stasio, G. Multiple Scattering Calculations of Bonding and X-ray Absorption Spectroscopy of Manganese Oxides. *J. Phys. Chem. A* **2003**, *107*, 2839–2847.
- (51) Mandal, S.; Cohen, R. E.; Haule, K. Valence and Spin Fluctuations in the Mn-Doped Ferroelectric BaTiO<sub>3</sub>. *Phys. Rev. B* **2018**, *98*, No. 075155.
- (52) Weidman, M. C.; Goodman, A. J.; Tisdale, W. A. Colloidal Halide Perovskite Nanoplatelets: An Exciting New Class of Semiconductor Nanomaterials. *Chem. Mater.* **2017**, *29*, 5019–5030.
- (53) Mir, W. J.; Jagadeeswararao, M.; Das, S.; Nag, A. Colloidal Mn-Doped Cesium Lead Halide Perovskite Nanoplatelets. *ACS Energy Lett.* **2017**, *2*, 537–543.
- (54) Wang, J.; Sun, F.; Yang, S.; Li, Y.; Zhao, C.; Xu, M.; Zhang, Y.; Zeng, H. Robust Ferromagnetism in Mn-Doped MoS<sub>2</sub> Nanostructures. *Appl. Phys. Lett.* **2016**, *109*, No. 092401.
- (55) Turynska, L.; Hill, R. J.; Makarovsky, O.; Moro, F.; Knott, A. N.; Larkin, O. J.; Patane, A.; Meaney, A.; Christianen, P. C.; Fay, M. W.; Curry, R. J. Tuneable Paramagnetic Susceptibility and Exciton G-Factor in Mn-Doped PbS Colloidal Nanocrystals. *Nanoscale* **2014**, *6*, 8919–8925.
- (56) Wu, L.-Y.; Zhang, M.-R.; Feng, Y.-X.; Zhang, W.; Zhang, M.; Lu, T.-B. Two-Dimensional Metal Halide Perovskite Nanosheets for Efficient Photocatalytic CO<sub>2</sub> Reduction. *Solar RRL* **2021**, *5*, No. 2100263.
- (57) Shyamal, S.; Dutta, S. K.; Pradhan, N. Doping Iron in CsPbBr<sub>3</sub> Perovskite Nanocrystals for Efficient and Product Selective CO<sub>2</sub> Reduction. *J. Phys. Chem. Lett.* **2019**, *10*, 7965–7969.
- (58) Xu, Y.-F.; Yang, M.-Z.; Chen, H.-Y.; Liao, J.-F.; Wang, X.-D.; Kuang, D.-B. Enhanced Solar-Driven Gaseous CO<sub>2</sub> Conversion by CsPbBr<sub>3</sub> Nanocrystal/Pd Nanosheet Schottky-Junction Photocatalyst. *ACS Appl. Energy Mater.* **2018**, *1*, 5083–5089.
- (59) Feldmann, S.; Gangishetty, M. K.; Bravic, I.; Neumann, T.; Peng, B.; Winkler, T.; Friend, R. H.; Monserrat, B.; Congreve, D. N.; Deschler, F. Charge Carrier Localization in Doped Perovskite Nanocrystals Enhances Radiative Recombination. *J. Am. Chem. Soc.* **2021**, *143*, 8647–8653.
- (60) Biz, C.; Fianchini, M.; Gracia, J. Strongly Correlated Electrons in Catalysis: Focus on Quantum Exchange. *ACS Catal.* **2021**, *11*, 14249–14261.
- (61) Gracia, J.; Sharpe, R.; Munarriz, J. Principles Determining the Activity of Magnetic Oxides for Electron Transfer Reactions. *J. Catal.* **2018**, *361*, 331–338.
- (62) Gracia, J. Itinerant Spins and Bond Lengths in Oxide Electrocatalysts for Oxygen Evolution and Reduction Reactions. *J. Phys. Chem. C* **2019**, *123*, 9967–9972.
- (63) Gracia, J.; Munarriz, J.; Polo, V.; Sharpe, R.; Jiao, Y.; Niemantsverdriet, J. W. H.; Lim, T. Analysis of the Magnetic Entropy in Oxygen Reduction Reactions Catalysed by Manganite Perovskites. *ChemCatChem* **2017**, *9*, 3358–3363.
- (64) Zhao, W.; Su, R.; Huang, Y.; Wu, J.; Fong, C. F.; Feng, J.; Xiong, Q. Transient Circular Dichroism and Exciton Spin Dynamics in All-Inorganic Halide Perovskites. *Nat. Commun.* **2020**, *11*, No. 5665.
- (65) Li, J.; Pei, Q.; Wang, R.; Zhou, Y.; Zhang, Z.; Cao, Q.; Wang, D.; Mi, W.; Du, Y. Enhanced Photocatalytic Performance through Magnetic Field Boosting Carrier Transport. *ACS Nano* **2018**, *12*, 3351–3359.
- (66) Lin, J. X.; Thaomonpun, J.; Thongpool, V.; Chen, W. J.; Huang, C. H.; Sun, S. J.; Remes, Z.; Tseng, Y. T.; Liao, Y. F.; Hsu, H. S. Enhanced Photodegradation in Metal Oxide Nanowires with Co-Doped Surfaces under a Low Magnetic Field. *ACS Appl. Mater. Interfaces* **2021**, *13*, 23173–23180.

## □ Recommended by ACS

### Facet-Dependent Mn Doping on Shaped Co<sub>3</sub>O<sub>4</sub> Crystals for Catalytic Oxidation

Junemin Bae, Hyunjoo Lee, et al.  
AUGUST 20, 2021  
ACS CATALYSIS

READ ▶

### Manganese Doping in Cobalt Oxide Nanorods Promotes Catalytic Dehydrogenation

Qingping Ke, Xi Wang, et al.  
MARCH 02, 2020  
ACS SUSTAINABLE CHEMISTRY & ENGINEERING

READ ▶

### Interfacial Electronic and Structural Reorganization in Mn<sub>2</sub>Co<sub>2</sub>C/MnO for Enhancing Oxygen Evolution Kinetics and Active Sites

Tao Meng and Minhua Cao  
AUGUST 10, 2020  
ACS SUSTAINABLE CHEMISTRY & ENGINEERING

READ ▶

### Insights into the Redox Behavior of Pr<sub>0.5</sub>Ba<sub>0.5</sub>MnO<sub>3-δ</sub>-Derived Perovskites for CO<sub>2</sub> Valorization Technologies

Andrea Felli, Marta Boaro, et al.  
MAY 18, 2022  
ACS APPLIED ENERGY MATERIALS

READ ▶

Get More Suggestions >